The Astrophysical Journal, 880:147 (11pp), 2019 August 1 https://doi.org/10.3847/1538-4357/ab2adb

X-Ray and Radio Variabilities of PSR J2032+4127 near Periastron

C.-Y. Ng[1], W. C. G. Ho[2,3], E. V. Gotthelf[4], J. P. Halpern[4], M. J. Coe[5], B. W. Stappers[6], A. G. Lyne[6], K. S. Wood[7], and M. Kerr[8]
[1] Department of Physics, The University of Hong Kong, Pokfulam Road, Hong Kong; ncy@astro.physics.hku.hk
[2] Department of Physics and Astronomy, Haverford College, 370 Lancaster Avenue, Haverford, PA 19041, USA
[3] Mathematical Sciences, Physics and Astronomy, and STAG Research Centre, University of Southampton, Southampton SO17 1BJ, UK
[4] Columbia Astrophysics Laboratory, Columbia University, 550 West 120th Street, New York, NY 10027-6601, USA
[5] Physics and Astronomy, University of Southampton, Southampton SO17 1BJ, UK
[6] Jodrell Bank Centre for Astrophysics, School of Physics and Astronomy, University of Manchester, Manchester M13 9PL, UK
[7] Praxis Inc., Resident at the Naval Research Laboratory, Washington, DC 20375, USA
[8] Space Science Division, Naval Research Laboratory, Washington, DC 20375-5352, USA
Received 2019 February 20; revised 2019 June 4; accepted 2019 June 17; published 2019 August 5

Abstract

We present X-ray and radio monitoring observations of the gamma-ray binary PSR J2032+4127/MT91 213 during its periastron passage in late 2017. Dedicated *Chandra*, *XMM-Newton*, *NuSTAR* X-ray observations, and Very Large Array radio observations of this long orbit (50 yr), 143 ms pulsar/Be star system clearly revealed flux and spectral variability during the passage. The X-ray spectrum hardened near periastron, with a significant decrease in the power-law (PL) photon index from $\Gamma \approx 2$ to 1.2 and evidence of an increased absorption column density. We identified a possible spectral break at a few keV in the spectrum that suggests synchrotron cooling. A coincident radio and X-ray flare occurred one week after periastron, which is possibly the result of the pulsar wind interacting with the Be stellar disk and generating synchrotron radiation. However, a multiwavelength comparison indicates that the X-ray and radio spectra cannot be simply connected by a single PL component. Hence, the emission in these two energy bands must originate from different particle populations.

Key words: pulsars: individual (PSR J2032+4127) – stars: individual (MT91 213) – stars: neutron – X-rays: binaries – X-rays: individual (PSR J2032+4127)

1. Introduction

Gamma-ray binaries are an emerging class of interacting binaries that emit most of their radiation power in GeV and TeV energies (see Dubus 2013; Dubus et al. 2017 for reviews). These systems offer a unique perspective to study nonthermal emission processes at high energies. Most importantly, their variabilities along the binary orbit give a powerful diagnostic tool for the physical conditions of the outflows and the environment, providing dynamical and geometrical information that is otherwise not possible from isolated sources.

There are fewer than 10 gamma-ray binaries known and only two of them, PSRs J2032+4127 and B1259−63, have pulsations detected, which firmly established the pulsar nature of the compact objects. The pulsar spin parameters give direct constraints on the energy input from its wind, allowing detailed physical modeling (e.g., Takata et al. 2017; Petropoulou et al. 2018; Coe et al. 2019). PSR J2032+4127 (hereafter J2032) was first identified as a gamma-ray pulsar with the *Fermi Gamma-Ray Space Telescope* (Abdo et al. 2009) and then later detected in radio and X-rays (Camilo et al. 2009). It has a spin period of 143 ms and is associated with the TeV source J2032+4130 (Aliu et al. 2014). Long-term radio timing revealed a highly eccentric ($e = 0.98$) orbit of the pulsar around a Be star MT91 213 in Cygnus OB2 association, with a binary period of 52.4 yr (Lyne et al. 2015; Ho et al. 2017; B. W. Stappers et al. 2019, in preparation). *Gaia* parallax measurement of the companion star suggest a distance of $1.39^{+0.08}_{-0.06}$ kpc (Jennings et al. 2018).

J2032 was predicted to be at periastron on 2017 November 13 (MJD 58070.73; Coe et al. 2017; Ho et al. 2017; B. W. Stappers et al. 2019, in preparation), and it has been closely monitored at different wavelengths before and after that. In X-rays, we found a flux increase by ∼20 times from 2002 to 2016 and a rapid brightening since late 2015 (Ho et al. 2017). It was suggested that the brightening could be attributed to strong X-ray flares on weekly to monthly timescales with a slowly increasing baseline (Li et al. 2017). During the periastron passage, the X-ray flux showed a sharp dip, which was then followed by a 20 day long flare (Li et al. 2018; Coe et al. 2019). Since the X-ray emission is believed to originate from the interaction between the stellar wind and the pulsar wind, the flux variation could indicate changes in the wind conditions, such as magnetization (Takata et al. 2017), or could be due to geometrical effects (Petropoulou et al. 2018). In gamma-rays, J2032 showed a different behavior that is difficult to explain. The TeV flux increased by an order of magnitude and peaked at periastron, then dropped abruptly one week later, and the low state lasted for a few days (Abeysekara et al. 2018). The GeV flux, however, exhibited no variability over the same period (Li et al. 2018). All these are not well modeled by current theories (e.g., Takata et al. 2017; Bednarek et al. 2018).

In this paper, we report on our monitoring campaign of J2032 in X-rays and radio, using the *Chandra X-ray Observatory*, *XMM-Newton*, *NuSTAR*, and the Jansky Very Large Array (VLA). Compared to the *Swift* X-ray results reported in previous studies, the sensitive instruments we used offered much better constraints on the spectral parameters, enabling us to determine not only the light curve but also spectral variabilities of the source near periastron.

2. Observations and Data Analysis

2.1. Chandra X-Ray Observatory

We carried out new *Chandra* ACIS-S observations between 2017 February and 2018 October in timed exposure mode with

Table 1
X-Ray Observations of J2032 Used in This Study

Obs. Date	ObsID	MJD	True Anomaly (°)	Net Exposure (ks)	Net Count Rate[a] (ks^{-1})	$f^{u.l.}_{p,N=1}$ [b] (%)	$f^{u.l.}_{p,N=1000}$ [b] (%)
Chandra							
2017 Feb 1	19607	57785.4	27.2	26.8	66.8	⋯	⋯
2017 May 28	19700	57901.8	33.6	28.6	143.9	⋯	⋯
2017 Aug 29	19701	57994.2	46.0	28.6	129.0	⋯	⋯
2017 Nov 3	19702	58060.4	102.1	19.1	114.8	⋯	⋯
2017 Nov 5	20836	58062.9	110.7	9.6	98.9	⋯	⋯
2018 Jan 9	19608	58128.2	307.7	29.0	108.5	⋯	⋯
2018 Mar 16	19698	58193.8	321.8	29.2	35.4	⋯	⋯
2018 Aug 19	20599	58349.6	332.6	27.7	15.5	⋯	⋯
2018 Oct 2	20848	58393.6	334.2	26.3	4.1	⋯	⋯
XMM-Newton							
2017 Oct 23	0801910201	58050.1	79.9	22.3	488.2	4.9	7.2
2017 Nov 5	0801910301	58063.0	111.0	16.4	261.2	8.0	11.7
2017 Nov 13	0801910401	58070.7	178.0	10.9	241.2	10.2	15.0
2017 Nov 22	0801910501	58079.3	252.1	13.9	551.4	5.8	8.5
2017 Dec 4	0801910601	58091.9	280.9	10.9	413.5	7.6	11.2
NuSTAR							
2017 Oct 23	30302002002	58050.2	80.1	37.9	182.1	6.5	9.5
2017 Nov 5	90302321002	58062.9	110.5	39.8	98.3	9.0	13.3
2017 Nov 13	30302002004	58070.5	177.7	42.7	82.7	9.6	14.2
2017 Nov 21	90302321004	58079.2	251.6	40.0	184.0	6.2	9.1
2017 Dec 4	30302002006	58092.2	281.2	41.5	130.7	7.6	11.1

Notes.
[a] In an energy range of 0.5–8 keV for *Chandra*, 0.5–10 keV for *XMM-Newton*, and 2–79 keV for *NuSTAR*. The *XMM-Newton* values are for the PN only, and the *NuSTAR* values are the sum from the FPMA and FPMB detectors.
[b] 3σ upper limits on the pulsed fraction, assuming a sinusoidal signal. $f^{u.l.}_{p,N=1}$ and $f^{u.l.}_{p,N=1000}$ correspond to 1 and 1000 search trials, respectively.

1/4 subarray. This gave a frame time of 0.8 s such that pileup is not an issue ($\lesssim$3% even when the source was brightest). The observation parameters are listed in Table 1. Data reduction was performed with CIAO 4.10 and CALDB 4.8.1. We first reprocessed the data using the task `chandra_repro`, then checked that there was no background flaring during the exposure. We generated light curves of J2032 but did not find any significant short-term variability between the frame time and the exposure time, i.e., for a timescale of $\sim$1 s to a few 10^4 s.

We extracted the spectrum of J2032 from a 5″ radius aperture and the background spectrum from nearby source-free regions. A large aperture was chosen to enclose most of the source flux, since the background is generally negligible. We grouped the spectra to at least 20 counts per bin, except for the last observation, which was grouped at 15 due to the low count rate, and performed spectral analysis using the *Sherpa* package. We fit the pulsar spectra in the 0.5–8 keV range with an absorbed power-law (PL) model. The absorption cross section and element abundances given by Wilms et al. (2000) are adopted. Finally, uncertainties in flux are estimated with Monte Carlo simulations.

2.2. XMM-Newton *and* NuSTAR

In addition to *Chandra*, we obtained five coordinated *XMM-Newton* and *NuSTAR* observations of J2032, taken on the day of periastron passage, and one and three weeks before and after that. The observation parameters are listed in Table 1. For *XMM-Newton*, the PN camera operated in the small window mode with a high time resolution of 6 ms, while the MOS cameras were in the large window mode with 0.9 s time resolution. The data reduction was performed with SAS v.15 and the most up-to-date calibration files. We followed the standard pipeline processing procedure and then filtered out time periods with high background. The resulting exposure times are listed in Table 1. The *NuSTAR* observations have a time resolution of better than 3 ms and the data reduction was performed using the standard processing pipeline in the latest version of NuSTARDAS.

For timing analysis, we extracted *XMM-Newton* counts in the 0.5–10 keV range from a 0.′5 radius aperture and *NuSTAR* counts in 20–30 keV from a 1′ radius aperture to generate light curves. The source count rates are found to be nearly constant over an observation and shorter timescales, with rms fluctuations of less than two times the mean statistical error (i.e., rms $\leqslant 2\bar{\sigma}$). This is confirmed by fast Fourier transforms of each data set that show little evidence of red noise or enhanced white noise. We also performed a pulsation search using *XMM-Newton* PN and *NuSTAR* events. Photon arrival times were converted to barycentric dynamical time (TDB) using the DE405 solar system ephemeris. The arrival times were further adjusted to account for binary motion of the pulsar. We searched for periodic signals over a small range of frequency near the pulsar period from radio timing (B. W. Stappers et al. 2019, in preparation). We tried the Z_1^2 test and also the χ^2 test with 10 phase bins, but no signals were found. The 3σ upper limits on the pulsed fraction for a putative sinusoidal signal are given in Table 1, after taking into account the background estimate and the number of search trials.

We extracted the *XMM-Newton* spectra of J2032 from a circular aperture of 0.′5 radius. There are four background X-ray sources in the aperture (see Figure 2), but the contamination should be negligible, given their low count

Table 2
VLA Observations of J2032 Used in This Study

Obs. Date	MJD	Array	Band	No. of Antennas	Center Freq. (GHz)	Bandwidth (GHz)	Integration Time (minutes)
2017 Aug 14	57979.2	C	*S*	27	3	2	23.7
2017 Sep 3	57999.4	B	*L*, *S*, *C*, *X*	27	1.52, 3, 5.5, 9	1, 2, 2, 2	7.0, 3.7, 3.7, 3.7
2017 Oct 24	58050.1	B	*L*, *S*, *C*, *X*	25	1.52, 3, 5.5, 9	1, 2, 2, 2	7.0, 3.8, 3.6, 3.6
2017 Nov 7	58064.1	B	*L*, *S*, *C*, *X*	27	1.52, 3, 5.5, 9	1, 2, 2, 2	6.9, 3.8, 3.6, 3.6
2017 Nov 13	58070.1	B	*L*, *S*, *C*, *X*	25	1.52, 3, 5.5, 9	1, 2, 2, 2	7.0, 3.7, 3.7, 3.7
2017 Nov 21	58078.9	B	*L*, *S*, *C*, *X*	27	1.52, 3, 5.5, 9	1, 2, 2, 2	6.9, 4.9, 4.2, 4.2
2017 Dec 3	58090.1	B	*L*, *S*, *C*, *X*	26	1.52, 3, 5.5, 9	1, 2, 2, 2	7.0, 3.7, 3.7, 3.7

rates (see the Appendix). The MOS background was extracted from an annular region with radii between 1′ and 2′ centered on the pulsar, and the PN background was from a 1′ radius circle offset by 1.′7 along the CCD readout direction. The *NuSTAR* source and background spectra were extracted from a 0.′8 radius circular region and an annular region between 1.′2 and 1.′9, respectively. We merged the *XMM-Newton* MOS spectra taken in the same day for a joint analysis, and did the same for the two *NuSTAR* FPM detectors. The source spectra were grouped with a minimum of 100 counts per bin and then fit using the *XSPEC* package.

We first fit the *XMM-Newton* spectra using the same model and energy range as the *Chandra* analysis above for a direct comparison. We then performed a joint fit to the *XMM-Newton* and *NuSTAR* spectra in the 0.5–10 keV and 3–79 keV energy ranges, respectively. An absorbed PL model was employed. We linked the column density ($N_{\rm H}$) and the PL photon index (Γ) of all spectra at each epoch, but allowed different PL normalizations to account for any cross-instrument flux miscalibrations. The fitting results are formally acceptable with reduced χ^2 values from 1.1 to 1.5. The normalizations between different instruments are consistent to within 5%. The best-fit spectra and residuals are shown in the left panel of Figure 1. There is a hint of systematic trend in the residuals, suggesting that a more complex spectral model may be needed. We therefore tried a broken PL model. This improves the fits and gives lower reduced χ^2 values of 0.9–1.1. The results are plotted in the right panels of Figure 1. The broken PL fit clearly reduces the residuals, particularly at low energy. We performed an F-test and confirmed that the additional component is statistically significant.

2.3. VLA

We carried out six new radio observations of J2032 with the VLA. Except the first one, the remaining five were taken within a couple days of the *XMM-Newton* and *NuSTAR* observations. The VLA was in the B array configuration, and the data were taken in the *L*, *S*, *C*, and *X* bands, covering a frequency from 1 to 10 GHz. In addition, we analyzed archival data observed earlier in 2017 in the *S* band with the C array configuration. The observation parameters are listed in Table 2. The time resolution was 3 s in all data, too low to resolve the pulsar spin period. Standard calibrators, either 3C 48, 3C 138, or 3C 286 were observed for absolute flux density scale, delay, and bandpass calibrations. A nearby phase calibrator J2007+4029 was observed for gain calibration. We also observed J1407 +2827 and 3C 147 for polarization calibration. Note that for the 2017 Nov 13 observation, 3C 147 was used as the primary calibrator since the 3C 138 data were severely contaminated by RFI.

All data reduction was done with CASA 5.1. We first applied the VLA calibration pipeline for basic flagging and calibration, then performed additional flagging when needed. We formed the radio images and carried out deconvolution with the task `tclean`. Briggs weighting with parameter robust = 0.5 was used to form *L* and *S* band images, while natural weighting was used for *C* and *X* bands. These weights were chosen to optimize the signal-to-noise ratio to boost the detection sensitivity. The final intensity maps have rms noise levels of $\sim$50 μJy beam^{-1} in the *L* band, $\sim$20 μJy beam^{-1} in the *S* band, and $\sim$15 μJy beam^{-1} in *C* and *X* bands. The beam size ranges from $\sim$4″ FWHM in the *L* band to $\sim$1″ FWHM in the *X* band. Finally, we generated polarization images for the 2017 November 21 observation, when the pulsar was brightest. However, no polarization signal was found.

3. Results

3.1. X-Rays

Figure 2 shows an exposure-corrected X-ray image of the field of J2032, generated by coadding all on-axis *Chandra* observations, including those used in this study and in our previous work (Ho et al. 2017). There is no obvious extended emission surrounding the pulsar. We plotted the radial count profile of the pulsar and found that it is consistent with a model PSF simulated by ChaRT.[9] We were unable to confirm the large-scale ($\sim$1.′6 diameter) diffuse emission reported in previous studies (Mukherjee et al. 2007; Camilo et al. 2009). However, we note that many of the *Chandra* exposures were taken in the subarray mode with a small field of view ($\sim$2′). J2032 was also very bright during most of the *Chandra* and *XMM-Newton* observing epochs such that dust scattering could be a potential issue. All these preclude a sensitive search for large-scale X-ray structure.

J2032 was clearly detected in all X-ray observations. It exhibited significant brightness variation between epochs. The best-fit spectral parameters to the *Chandra* and *XMM-Newton* spectra are listed in Table 3. The flux obtained from different *XMM-Newton* cameras are well matched to within 5%. We therefore report only the average values in the table. A simple absorbed PL provides adequate fits to the X-ray spectra at different epochs, although the parameters are not very well constrained in the last *Chandra* observation due to the small number of counts. The *Chandra* and *XMM-Newton* results are generally consistent. In Table 4 we report results from the joint *XMM-Newton* and *NuSTAR* spectral fits. As mentioned, the fits

[9] http://cxc.harvard.edu/ciao/PSFs/chart2/index.html

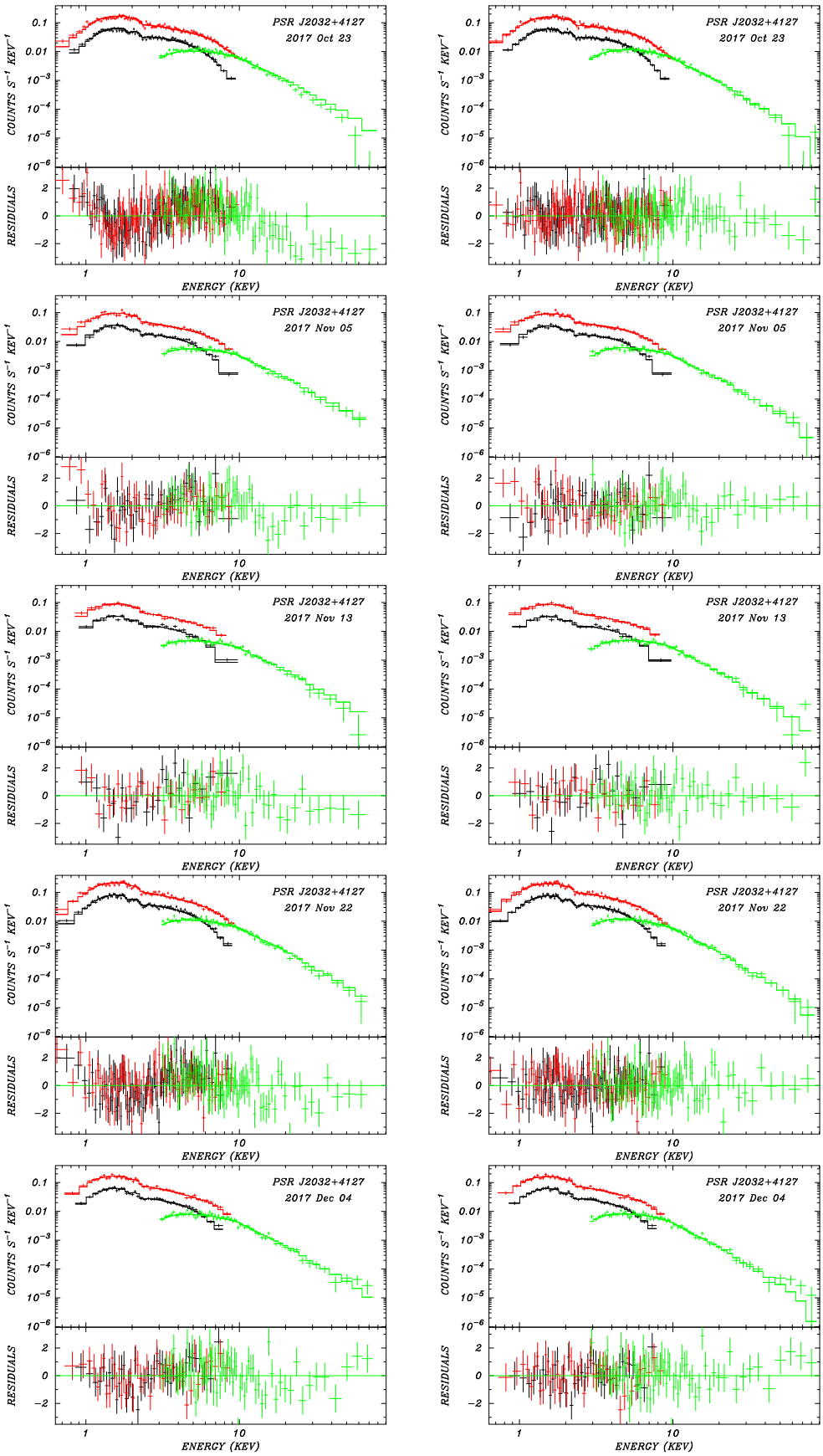

Figure 1. Joint fits to the *XMM-Newton* and *NuSTAR* spectra of J2032, with an absorbed single PL model (left) and an absorbed broken PL model (right).

Table 3
Single PL Fits to the *Chandra* and *XMM-Newton* Spectrum of J2032

Obs. Date	$N_{\rm H}$ (10^{22} cm^{-2})	Γ	Abs. Flux (10^{-13} erg cm^{-2} s^{-1})	χ^2_ν/dof
Chandra (Single PL)				
2017 Feb 1	1.6 ± 0.2	2.1 ± 0.2	9.6 ± 0.6	1.12/73
2017 May 28	1.5 ± 0.1	1.7 ± 0.1	24.7 ± 1.1	0.78/157
2017 Aug 29	$1.3^{+0.2}_{-0.1}$	1.4 ± 0.1	$25.2^{+1.1}_{-1.2}$	0.91/145
2017 Nov 3	1.4 ± 0.2	1.2 ± 0.1	$25.5^{+1.5}_{-1.7}$	1.02/92
2017 Nov 5	1.3 ± 0.4	1.2 ± 0.2	$21.8^{+2.0}_{-2.2}$	1.17/42
2018 Jan 9	1.5 ± 0.2	1.6 ± 0.1	$20.0^{+1.0}_{-1.1}$	0.78/126
2018 Mar 16	$1.0^{+0.3}_{-0.2}$	1.6 ± 0.2	6.1 ± 0.6	0.83/45
2018 Aug 19	$1.1^{+0.5}_{-0.4}$	$2.1^{+0.4}_{-0.3}$	2.0 ± 0.3	1.29/18
2018 Oct 2	$1.0^{+1.3}_{-0.8}$	$1.5^{+0.9}_{-0.7}$	$0.6^{+0.2}_{-0.3}$	0.95/5
XMM-Newton (Single PL)				
2017 Oct 23	1.02 ± 0.05	1.19 ± 0.04	31.0 ± 0.6	1.0/186
2017 Nov 5	$0.96^{+0.09}_{-0.08}$	1.24 ± 0.06	$16.5^{+0.5}_{-0.6}$	1.1/78
2017 Nov 13	$0.92^{+0.13}_{-0.12}$	1.29 ± 0.09	14.6 ± 0.6	1.1/45
2017 Nov 22	1.02 ± 0.05	1.41 ± 0.04	32.4 ± 0.7	1.2/149
2017 Dec 4	$0.98^{+0.08}_{-0.07}$	1.43 ± 0.06	$24.3^{+0.7}_{-0.8}$	0.8/81

Note. All uncertainties are at the 90% confidence level. The best-fit absorbed flux is in the 0.5–8 keV energy range, and the *XMM-Newton* flux are the average values from all three cameras.

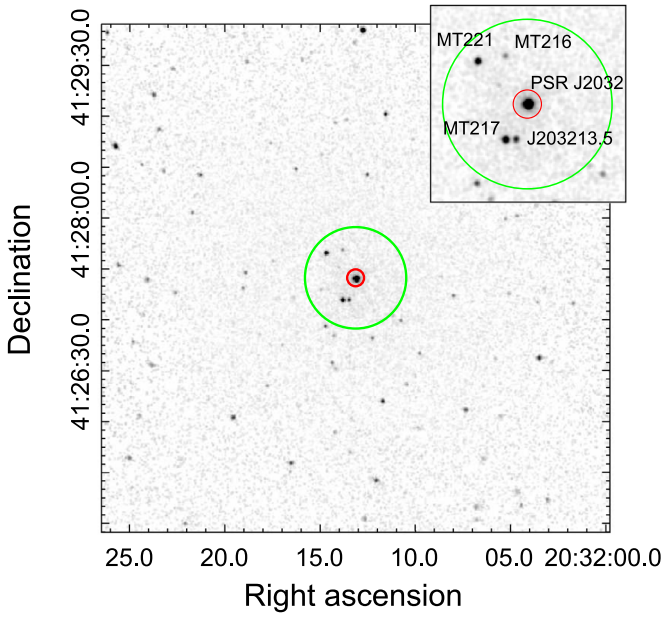

Figure 2. Exposure-corrected *Chandra* X-ray image of the field centered on J2032 in the 0.5–7 keV range, lightly smoothed to 2″ resolution. The red and green circles have radii of 5″ and 30″ that indicate the extraction regions for *Chandra* and *XMM-Newton* spectral analysis, respectively. Inset: zoom-in of the image showing four nearby background sources: MT91 221, MT91 216, MT91 217, and CXOU J203213.5+412711 (see the Appendix).

with a simple PL are acceptable, but a broken PL gives better results and the improvement is statistically significant as shown by an F-test. In the latter model, a spectral break around 4–8 keV was found and the PL photon index changes by $\Delta\Gamma = 0.3$–0.5 across the break.

As we did not try fitting a broken PL to the *Chandra* data due to the low sensitivity of the telescope at high energies, for the rest of the section, we focus on the single PL fit in order to investigate the spectral evolution of J2032. The best-fit spectral parameters at different epochs are plotted in Figure 3. The column density shows a hint of a decreasing trend prior to periastron, but after that, the variability is less clear due to limited sensitivity of the measurements. On the other hand, the PL photon index exhibited a more significant change. It decreased from $\Gamma \approx 2$ in early 2017 to $\approx$1.2 around periastron, then rose back with a similar timescale. The flux evolution is plotted in Figure 3. It peaked at 3.5×10^{-12} erg cm^{-2} s^{-1} one week after periastron. After correcting for interstellar absorption and scaling to a distance of 1.39 kpc, this value corresponds to a luminosity of 8.7×10^{32} erg s^{-1} in 2–10 keV range. In Figure 4, the spectral parameters are plotted against the true anomaly, and they show similar evolution trends.

We can compare our results with the X-ray light curve from *Swift*. The latter was converted from the count rates reported by Coe et al. (2019), assuming average $N_{\rm H} = 1.15 \times 10^{22}$ cm^{-2} and $\Gamma = 1.47$ from the *XMM-Newton* and *NuSTAR* fits. The results are plotted in Figure 5. The flux measurements from different telescopes are consistent and there are obvious fluctuations of the pulsar flux on a daily timescale. The largest variability was over a factor of $\sim$2, between periastron and one week after, i.e., the third and fourth *XMM-Newton*/*NuSTAR* observations. Over a longer timescale, the X-ray flux gradually increased before periastron, then showed a drastic dip at periastron and quick recovery, followed by a long declining trend by more than an order of magnitude in a year (see Li et al. 2018; Coe et al. 2019).

3.2. Radio

At radio frequencies, J2032 was detected in all *L*-band VLA images, while the emission sometimes fell below the observation sensitivity limits at higher frequencies. The results are listed in Table 5 and plotted in Figures 5 and 6. No extended radio emission was found, and J2032 is consistent with a point

Table 4
Joint *XMM-Newton* and *NuSTAR* Fits to the Spectrum of J2032

Obs. Date	$N_{\rm H}$ (10^{22} cm^{-2})	Γ/Γ_1	Γ_2	$E_{\rm break}$ (keV)	Abs. Flux (10^{-13} erg cm^{-2} s^{-1})	χ^2_ν/dof
XMM-Newton and *NuSTAR* (Single PL)						
2017 Oct 23	1.25 ± 0.07	1.39 ± 0.04	...	...	34.0 ± 0.4	1.45/273
2017 Nov 5	1.13 ± 0.10	1.40 ± 0.06	...	...	17.9 ± 0.3	1.11/133
2017 Nov 13	1.12 ± 0.13	1.45 ± 0.07	...	...	15.6 ± 0.3	1.16/95
2017 Nov 22	1.16 ± 0.06	1.54 ± 0.04	...	...	34.5 ± 0.4	1.34/233
2017 Dec 4	1.11 ± 0.08	1.57 ± 0.05	...	...	25.3 ± 0.4	1.18/151
XMM-Newton and *NuSTAR* (Broken PL)						
2017 Oct 23	0.97 ± 0.06	1.13 ± 0.06	1.63 ± 0.06	5.3 ± 0.7	35.3 ± 0.4	0.91/271
2017 Nov 5	0.91 ± 0.09	1.18 ± 0.07	1.55 ± 0.09	4.7 ± 0.8	18.4 ± 0.3	0.92/131
2017 Nov 13	0.93 ± 0.08	1.30 ± 0.17	1.70 ± 0.12	8.1 ± 2.4	16.2 ± 0.3	0.99/93
2017 Nov 22	0.93 ± 0.11	1.26 ± 0.06	1.65 ± 0.08	3.8 ± 1.0	35.2 ± 0.4	1.10/231
2017 Dec 4	1.00 ± 0.06	1.46 ± 0.10	1.73 ± 0.08	6.4 ± 1.7	25.9 ± 0.4	1.10/149

Note. All uncertainties are at the 90% confidence level. The best-fit absorbed flux is the average values from different cameras in the 2–10 keV energy range.

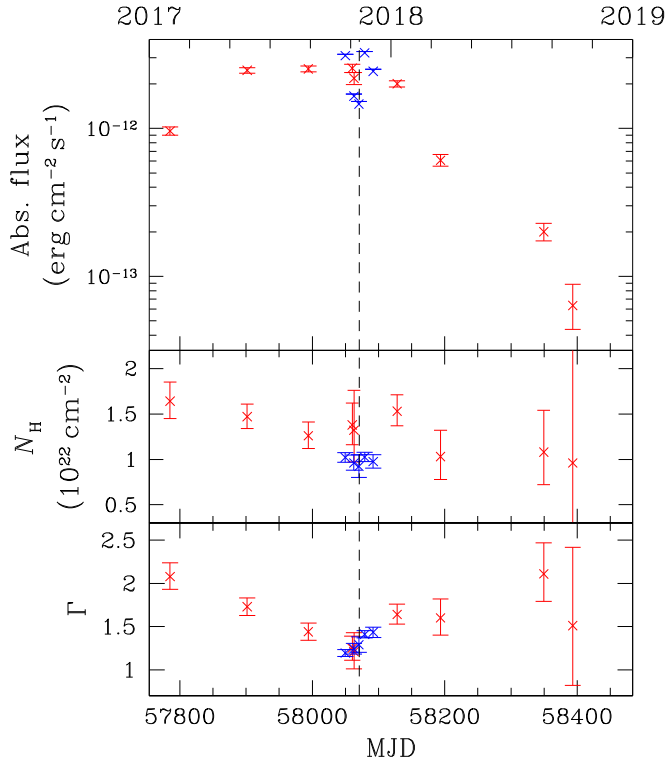

Figure 3. Best-fit X-ray flux, column density ($N_{\rm H}$), and photon index (Γ) of J2032, obtained from the single PL model as listed in Table 3. The red and blue data points indicate the *Chandra* and *XMM-Newton* results, respectively. The top panel shows the absorbed flux in the 0.5–8 keV energy range. The vertical dashed line marks the date of periastron passage.

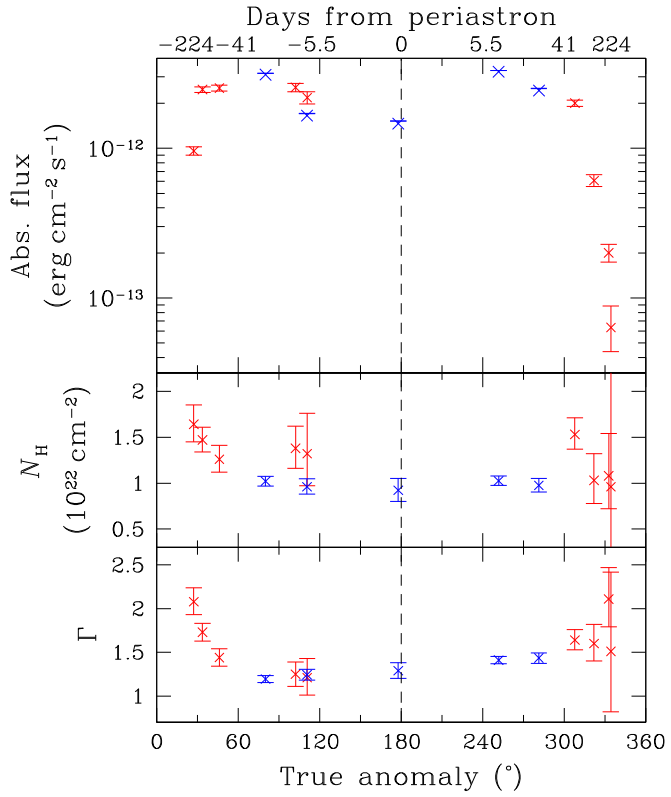

Figure 4. Same as Figure 3 but plotted against true anomaly.

source in all VLA images. Similar to the X-ray emission, the radio flux exhibited a dip at periastron but increased drastically by an order of magnitude one week after. In the last VLA observation taken three weeks following periastron passage, the flux density at the *L* band has returned to the pre-periastron level, but at higher frequencies it remained about a factor of two higher. In the bottom panel of Figure 5 we also plot the pulsed flux density of J2032 at the *L* band for comparison, which began to drop a few days after periastron and stayed low for about 20 days (B. W. Stappers et al. 2019, in preparation).

Finally, we show in Figure 6 the radio spectrum at different epochs. When the emission was brightest one week after periastron, its spectrum is well fit by a PL with spectral index $\alpha = -0.71$ ($S_\nu \propto \nu^\alpha$). The spectrum was, however, more complicated in other epochs and cannot be described by a simple PL.

4. Discussion

Our new observations offered sensitive spectral measurements of J2032. We show that the X-ray spectrum is well fit

Table 5
Radio Flux Densities of J2032 Measured with the VLA

Obs. Date	Flux Density[a] (mJy)			
	L band	*S* band	*C* band	*X* band
2017 Aug 14	...	0.080 ± 0.012	...	...
2017 Sep 3	0.18 ± 0.05	0.09 ± 0.02	<0.05	<0.05
2017 Oct 24	0.17 ± 0.05	<0.05	<0.04	<0.04
2017 Nov 7	0.17 ± 0.04	0.033 ± 0.016	0.030 ± 0.014	0.035 ± 0.014
2017 Nov 13	0.08 ± 0.06	0.040 ± 0.019	0.050 ± 0.015	<0.05
2017 Nov 21	1.17 ± 0.05	0.776 ± 0.016	0.490 ± 0.013	0.345 ± 0.011
2017 Dec 3	0.15 ± 0.06	0.146 ± 0.018	0.091 ± 0.014	0.059 ± 0.012

Notes.
[a] The uncertainties are estimated from the rms noise of the intensity maps. In the case of nondetection, 3σ limits (i.e., three times of the rms values) are reported.

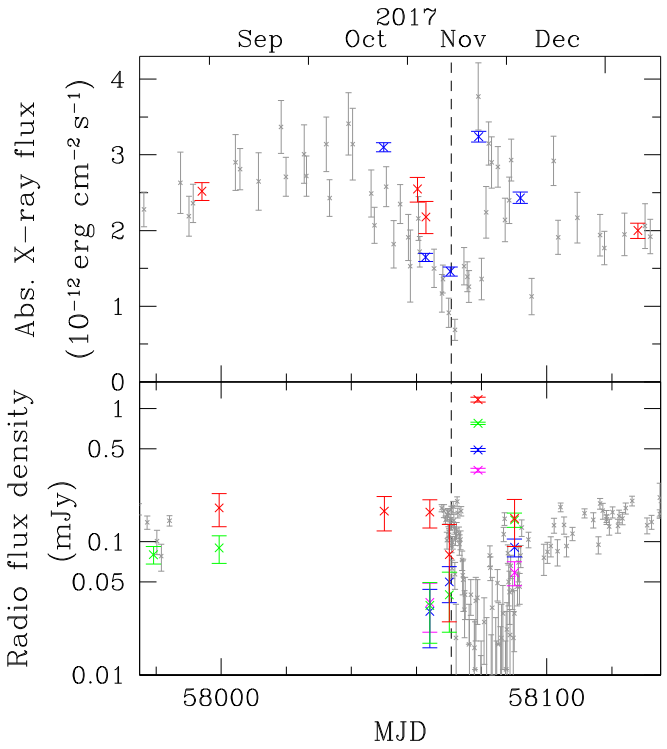

Figure 5. Top: X-ray flux of J2032 as in Figure 3 (red: *Chandra*; blue: *XMM-Newton*+*NuSTAR*) compared with the *Swift* light curve (gray) around periastron. All these are absorbed flux in the 0.5–8 keV range. Bottom: radio flux densities of J2032 over the same period. The VLA detections at the *L*, *S*, *C*, and *X* bands are shown in red, green, blue, and magenta, respectively. The gray data points indicate the pulsed flux density at the *L* band for comparison (B. W. Stappers et al. 2019, in preparation). The vertical dashed line marks the date of periastron passage.

with a PL. The small photon index ($\Gamma < 2$) rules out blackbody emission, indicating nonthermal distribution of the emitting particles. Together with the lack of X-ray pulsations near periastron and the strong flux variability, these suggest that the emission originated near the intrabinary shock between the stellar and pulsar winds, and is likely to be synchrotron radiation from particles accelerated in the shock. We showed that the X-ray PL spectrum flattened from $\Gamma \approx 2$ to 1.2 at periastron. For synchrotron emission, this corresponded to a change of particle distribution $dN/dE \propto E^{-p}$ from $p = 3$ to 1.4. A steeper spectrum indicates that the injected particles had sufficient time to cool before escaping the radiation zone when the pulsar was far from periastron.

In the following discussion, we assume that MT91 213 has mass $M_* = 15\,M_\odot$ and radius $R_* = 8\,R_\odot$ (Vacca et al. 1996; Hohle et al. 2010; Ho et al. 2017). Velocity of the radial wind is estimated to be

$$v_{\rm w} \sim \left(\frac{2GM_*}{R_*}\right)^{1/2} \approx 850\ {\rm km\ s^{-1}}. \quad (1)$$

We will take $v_{\rm w} = 10^3\,{\rm km\,s^{-1}}$ for simplicity. Observations and simulations suggest a mass-loss rate of $\dot{M}_{\rm ej} \sim 10^{-9}$–$10^{-8}\ M_\odot\,{\rm yr^{-1}}$ for Be stars (Snow 1981; Puls et al. 2008; Krtička 2014), implying wind density

$$\rho_0 = \frac{\dot{M}_{\rm ej}}{4\pi R_*^2 v_{\rm w}} \sim 10^{-16}\text{–}10^{-15}\ {\rm g\ cm^{-3}}. \quad (2)$$

If the stellar wind density decreases with distance r from the star as $\rho_{\rm w}(r) = \rho_0(R_*/r)^2$ (e.g., Petropoulou et al. 2018), we can determine the wind shock distance $r_{\rm sh}$ from the pulsar by pressure balance

$$\frac{\dot{E}}{4\pi c r_{\rm sh}^2} = \rho_{\rm w} v_{\rm w}^2 = \rho_0\left(\frac{R_*}{r_p - r_{\rm sh}}\right)^2 v_{\rm w}^2, \quad (3)$$

where $\dot{E} = 1.6 \times 10^{35}\,{\rm erg\,s^{-1}}$ is the pulsar spindown luminosity and r_p is the periastron separation. Using the typical neutron star mass $M_{\rm NS} = 1.35\,M_\odot$ and the updated timing solution with orbital period of 19113.4 days and eccentricity of 0.9799 (B. W. Stappers et al. 2019, in preparation), we obtain $r_p = 0.71$ au. Solving the equation above gives

$$r_{\rm sh} = 2.9 \times 10^7\ {\rm km}\left(\frac{10^{-15}\ {\rm g\ cm^{-3}}}{\rho_0}\right)^{1/2}\left(\frac{10^3\ {\rm km\ s^{-1}}}{v_{\rm w}}\right). \quad (4)$$

This is much larger than the Bondi radius for accretion

$$r_{\rm B} \approx \frac{2GM_{\rm NS}}{v_{\rm w}^2} = 3.7 \times 10^5\ {\rm km}\left(\frac{10^3\ {\rm km\ s^{-1}}}{v_{\rm w}}\right)^2. \quad (5)$$

Here we took the wind velocity as the relative velocity, since the neutron star orbital velocity is always smaller than $v_{\rm w}$ even at periastron. We therefore do not expect significant accretion.

The *XMM-Newton*+*NuSTAR* spectral fits indicate a possible break of the PL spectrum at ~5 keV. This can be attributed to synchrotron cooling. Assuming energy equipartition, the

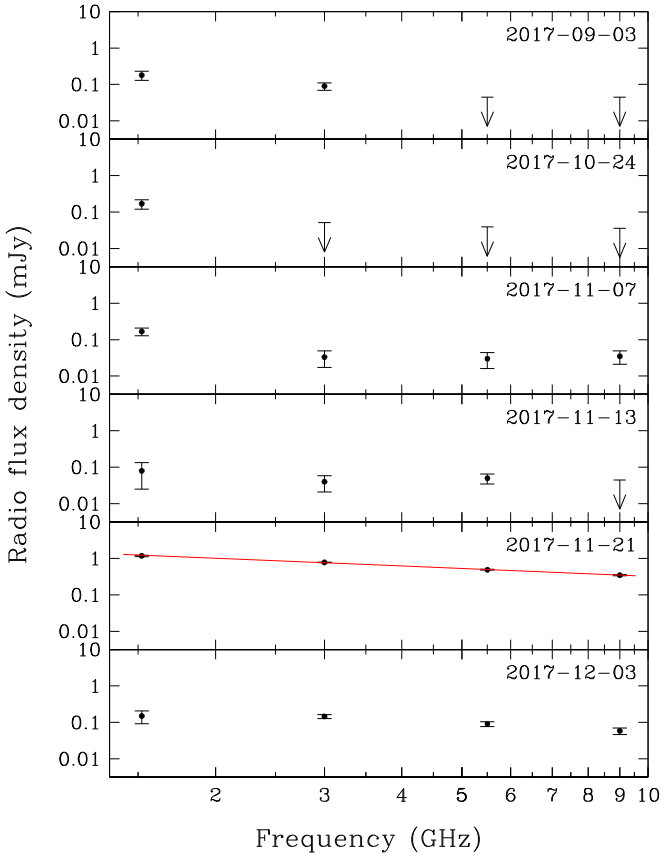

Figure 6. Radio spectrum of J2032 at different epochs measured with the VLA. In cases of nondetection, 3σ upper limits are plotted. The line shows the best-fit spectrum of $S_\nu \propto \nu^{-0.71}$ when the emission was brightest.

magnetic field of the wind at the shock is

$$B \sim (4\pi\rho_{\rm w} v_{\rm w}^2)^{1/2} = 0.8\ {\rm G}\left(\frac{\rho_0}{10^{-15}\ {\rm g\ cm^{-3}}}\right)^{1/2}\left(\frac{v_{\rm w}}{10^3\ {\rm km\ s^{-1}}}\right). \quad (6)$$

The post-shock particles are expected to have a flow speed of $c/3$ (Rees & Gunn 1974). If we take their travel time across the periastron distance as the synchrotron cooling time, we obtain a spectral break at ∼10 keV, comparable to our result. Finally, our new X-ray observations found an absorption column density $N_{\rm H} = 1.1 \times 10^{22}\,{\rm cm^{-2}}$. This is higher than the value $7.7 \times 10^{21}\,{\rm cm^{-2}}$ inferred from the color excess of MT91 213 (Camilo et al. 2009) and $3.4 \times 10^{21}\,{\rm cm^{-2}}$ from the pulsar dispersion measure (He et al. 2013). We speculate that part of the absorption could be contributed by the stellar wind

$$\Delta N_{\rm H} \sim \beta r_{\rm sh}\rho_{\rm w}/m_{\rm p}, \quad (7)$$

where β parameterizes the density enhancement due to the shock and $m_{\rm p}$ is hydrogen mass. For $\beta = 10^3$, $\Delta N_{\rm H} = 8 \times 10^{21}{\rm cm^{-2}}$, which could help explain the observed value.

We can compare J2032 with a similar system PSR B1259 −63/LS 2883 (hereafter B1259), the only other known gamma-ray binary consisting of a pulsar and a Be-type star (Johnston et al. 1992). It has a comparable periastron separation of 0.77 au but a much shorter orbital period of 3.4 yr (Negueruela et al. 2011; Miller-Jones et al. 2018). The X-ray light curve of B1259 peaked ∼20 days before and after periastron, corresponding to the times when the pulsar crossed the Be stellar disk (Chernyakova et al. 2014, 2015). This is different from the slowly rising peak of J2032 before periastron and the short-timescale flare after. It was argued that only the latter was caused by the pulsar passing through the disk (Li et al. 2018). On the other hand, both systems exhibited similar spectral variations. B1259 was also found to have $N_{\rm H}$ enhancement and hardened, with Γ changing from ∼2 to 1.5, near periastron (Chernyakova et al. 2006, 2015). High resolution *Chandra* observations revealed an extended X-ray feature moving away from B1259 at $2\farcs0 \pm 0\farcs3\ {\rm yr^{-1}}$, corresponding to a projected speed of $0.07c$ (Kargaltsev et al. 2014; Pavlov et al. 2015), and it can be attributed to the pulsar and stellar wind mixture ejected near periastron (Barkov & Bosch-Ramon 2016). For J2032, we did not find such extended emission in the entire $2'$ *Chandra* field of view, although our source is at a closer distance (1.39 kpc versus 2.6 kpc; Miller-Jones et al. 2018).

J2032 was previously claimed to show a hint of spectral variation, with $\Delta N_{\rm H} \approx 2 \times 10^{22}\,{\rm cm^{-2}}$ and $\Delta\Gamma \approx 0.8$ over two months in late 2016, by comparing between two different telescope observations (Li et al. 2017). In our study, we performed multiple observations using a single set of instruments but did not find such large variations in our observing period. As Figure 3 indicates, the *XMM-Newton* and *NuSTAR* flux varied by a factor of two between the high and low states near periastron, but the spectral parameters remained almost unchanged. This suggests that the previous finding could be due to cross-calibration issues.

In the radio band, Li et al. (2018) reported the detection of J2032 with the VLA in 2017 August, and the emission was suggested to originate from the pulsar magnetosphere. Our new observations support this picture. The VLA flux at the *L* band stayed roughly constant before periastron and was consistent with the pulsed value. At higher frequency, we argue that the pulsar wind emission could be relatively important, due to its flat spectrum (e.g., Kaspi et al. 2006). Its flux is also expected to vary along the binary orbit. When combining with the magnetospheric emission, these could possibly result in a complicated spectrum as shown in Figure 6.

A strong unpulsed emission component emerged about one week after periastron. It has flux density 10 times higher than the pulsed component and fast rising and decay times of less than a week each. We therefore consider it as a radio flare. Figure 5 shows that the flare coincided with the X-ray flare but decayed faster and nearly returned to the pre-periastron level after a week. The radio flare has a spectral index of $\alpha = -0.71$, suggesting that it could be synchrotron radiation (see Johnston et al. 2005). However, this is steeper than the X-ray spectrum obtained with a single PL ($\alpha_{\rm X} = 1 - \Gamma = -0.54$) fit and comparable to the high energy part of the broken PL fit ($1 - \Gamma_2 = -0.65$). We plot in Figure 7 the broadband spectral-energy distribution of J2032 during the flare. It is clear that the radio and X-ray spectra are not connected, suggesting that the two emission could arise from different particle populations.

The radio behavior of J2032 is very similar to that of B1259. Radio pulsations from the latter also ceased near periastron. This was suggested to be due to free–free absorption when the pulsar was behind the equatorial disk (Melatos et al. 1995). The radio and X-ray light curves of B1259 showed a good

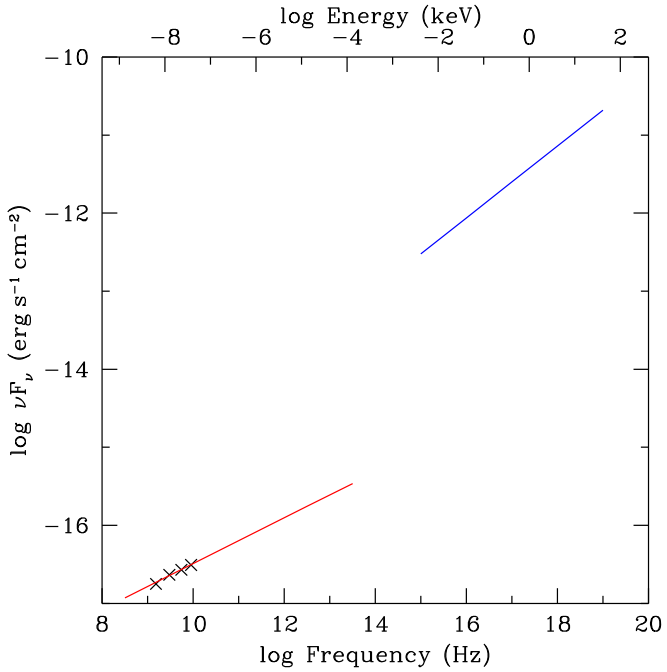

Figure 7. Spectral-energy distribution of J2032 during the X-ray and radio flare that occurred one week after periastron. The best-fit simple PL spectra to the radio and X-ray data are shown by the red and blue lines, respectively. The data points indicate the VLA measurements.

correlation (Chernyakova et al. 2014), with an unpulsed radio emission component which emerged during the X-ray flares before and after periastron. This emission has a radio spectral index of $\alpha = -0.6$, comparable to -0.71 for J2032 (Johnston et al. 2005). It was believed to originate from electrons accelerated by the intrabinary shock when B1259 moved through the stellar disk (Ball et al. 1999). For the case of J2032, although the disk of MT91 213 shrank near periastron such that it may not have directly interacted with the pulsar (see Coe et al. 2017; Kolka et al. 2017), we argue that the pulsar wind shock could possibly extend far enough to encounter the disk, or that the particle environment near the disk was sufficiently different.

As a final remark, Li et al. (2018) present the GeV light curve of J2032 and show that there is not a noticeable flare coinciding with the X-ray/radio flare we found at about one week post-periastron. However, it is worth noting that they used two-week bins for the light curve and thus are not able to resolve a GeV flare if one took place. On the other hand, such a GeV flare in J2032 would behave very differently from the very luminous and variable GeV flares of B1259, which take place around 20 days pre- and post-periastron (see, e.g., Johnson et al. 2018; Tam et al. 2018).

5. Conclusion

We studied the X-ray and radio emission properties of J2032 near the periastron passage in late 2017. Using new observations taken with *Chandra*, *XMM-Newton*, and *NuSTAR*, we showed that the X-ray emission of the system is nonthermal and it can be described by a PL with a possible break around a few keV. We found clear evidence of spectral variation in X-rays. The PL became harder at periastron, and there is a hint of increasing column density. We found no X-ray pulsations or short-timescale flux variabilities. In the radio band, we carried out VLA observations from 1 to 10 GHz and discovered that an unpulsed emission component emerged one week after periastron, at the same time as the X-ray flare. The spectral index of the emission suggests that it is synchrotron emission, likely resulting from the interaction of the pulsar with the Be stellar disk. For further investigation, detailed modeling is needed to quantitatively explain the observed flux and spectral behavior. This will provide insight into the particle acceleration process of the intrabinary shock.

We thank the referee for a careful reading and useful suggestions. C.Y.N. is supported by a GRF grant from the Hong Kong Government under HKU 17305416P. J.P.H. and E.V.G. acknowledge support from NASA through *XMM-Newton* grant 80NSSC18K0402. This work was also supported by *Chandra* Awards SAO GO7-18055X (J.P.H.) and GO8-19123X (W.C.G.H). *Chandra* grants are issued by the *Chandra* X-ray Center (CXC), which is operated by the Smithsonian Astrophysical Observatory for and on behalf of NASA under contract NAS8-03060. Pulsar observations with the Lovell Telescope are supported by a consolidated grant from the STFC. Work at NRL is supported by NASA.

This research is in part based on the data obtained from the *Chandra* Data Archive, and has made use of software provided by the CXC in the application packages CIAO, ChIPS, and Sherpa. This research has used the observations obtained with *XMM-Newton* and ESA science mission with instruments and contributions directly funded by the ESA member states and NASA. This research has also made use of data obtained with *NuSTAR*, a project led by Caltech, funded by NASA and managed by NASA/JPL, and has utilized the NUSTARDAS software package, jointly developed by the ASDC (Italy) and Caltech (USA). The National Radio Astronomy Observatory is a facility of the National Science Foundation operated under cooperative agreement by Associated Universities, Inc.

Facilities: CXO, *XMM*, *NuSTAR*, VLA.

Software: Sherpa (Freeman et al. 2001; Doe et al. 2007), XSPEC (Arnaud 1996), CIAO (v4.10; Fruscione et al. 2006), ChIPS (Germain et al. 2006), NUSTARDAS, SAS (v15; Gabriel et al. 2004), CASA (v5.1; McMullin et al. 2007).

Appendix
Net Count Rates of nearby X-Ray Sources

As shown in Figure 2, there are four background X-ray sources within 5″ of J2032, namely, MT91 216, MT91 217 (also known as Cyg OB2 4 and BD+40° 4219), MT91 221, and CXOU J203213.5+412711. These sources are covered by all *Chandra* observations. We estimated their counts from 2″ radius apertures and then subtracted background from nearby source-free regions. The resulting net count rates are listed in Table 6 and plotted in Figure 8. These sources showed significant X-ray variabilities, but they were all much fainter than J2032 near periastron passage. Therefore contamination in the *XMM-Newton* and *NuSTAR* spectra should be minimal. We did not perform detailed spectral analysis as there are too few counts.

We also report the X-ray light curve of a colliding wind binary, V729 Cyg (BD+40° 4220, Cyg OB2 5, Schulte 5), which is covered by the *Swift* field of view. We extracted the

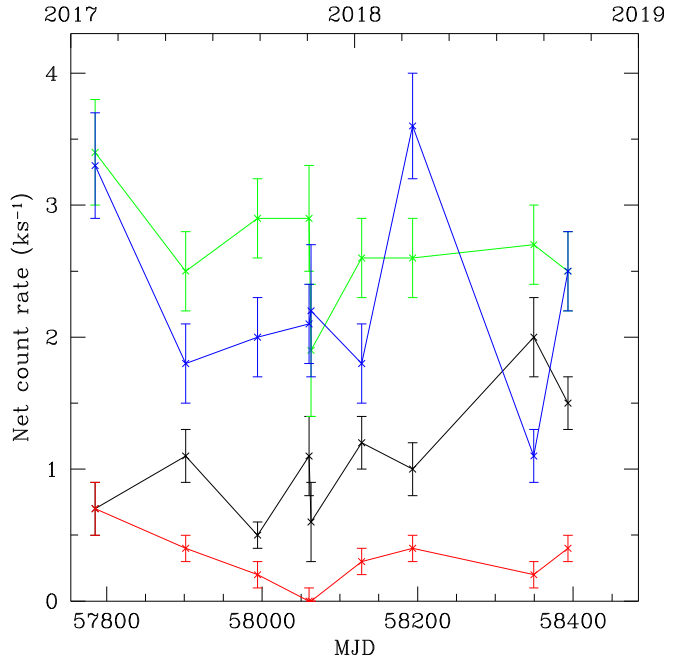

Figure 8. Background-subtracted *Chandra* count rates of sources near J2032 in 0.5–8 keV range. The red, green, blue, and black lines represent MT91 216, MT91 217, MT91 221, and CXOU J203213.5+412711, respectively.

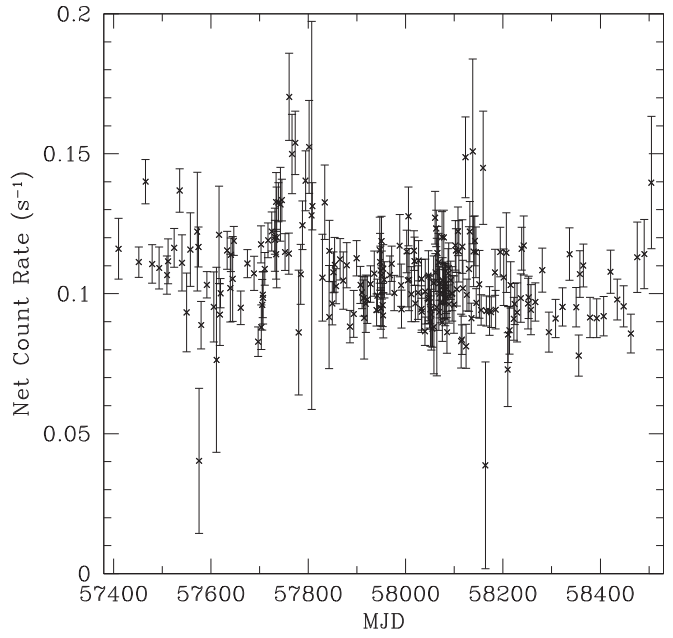

Figure 9. Background-subtracted *Swift* count rates of V729 Cyg in the 0.2–10 keV energy range.

count rate from 30″ radius source and background regions. The net count rate in 0.2–10 keV energy range is plotted in Figure 9. While this eclipsing binary has an orbital period of 6.6 days (Hall 1974), our X-ray light curve shows no obvious modulation in the 2–100 days range. We can place an upper limit of 1.4% for the amplitude of any variation based on a simple sinusoidal fit to the folded light curve at this precise period.

Table 6
Background-subtracted *Chandra* Count Rates of MT91 216, MT91 217, MT91 221, and CXOU J203213.5+412711 in 0.5–8 keV

Obs. Date	Net Count Rate (ks^{-1})			
	J203213.5	MT91 216	MT91 217	MT91 221
2017 Feb 1	0.7 ± 0.2	0.7 ± 0.2	3.4 ± 0.4	3.3 ± 0.4
2017 May 28	1.1 ± 0.2	0.4 ± 0.1	2.5 ± 0.3	1.8 ± 0.3
2017 Aug 29	0.5 ± 0.1	0.2 ± 0.1	2.9 ± 0.3	2.0 ± 0.3
2017 Nov 3	1.1 ± 0.3	0.0 ± 0.1	2.9 ± 0.4	2.1 ± 0.3
2017 Nov 5	0.6 ± 0.3	0.0 ± 0.0	1.9 ± 0.5	2.2 ± 0.5
2018 Jan 9	1.2 ± 0.2	0.3 ± 0.1	2.6 ± 0.3	1.8 ± 0.3
2018 Mar 16	1.0 ± 0.2	0.4 ± 0.1	2.6 ± 0.3	3.6 ± 0.4
2018 Aug 19	2.0 ± 0.3	0.2 ± 0.1	2.7 ± 0.3	1.1 ± 0.2
2018 Oct 2	1.5 ± 0.2	0.4 ± 0.1	2.5 ± 0.3	2.5 ± 0.3

ORCID iDs

C.-Y. Ng https://orcid.org/0000-0002-5847-2612
W. C. G. Ho https://orcid.org/0000-0002-6089-6836
E. V. Gotthelf https://orcid.org/0000-0003-3847-3957
J. P. Halpern https://orcid.org/0000-0003-4814-2377
M. J. Coe https://orcid.org/0000-0002-0763-8547
B. W. Stappers https://orcid.org/0000-0001-9242-7041
A. G. Lyne https://orcid.org/000-0002-4799-1281
M. Kerr https://orcid.org/0000-0002-0893-4073

References

Abdo, A. A., Ackermann, M., Ajello, M., et al. 2009, Sci, 325, 840
Abeysekara, A. U., Benbow, W., Bird, R., et al. 2018, ApJL, 867, L19
Aliu, E., Aune, T., Behera, B., et al. 2014, ApJ, 788, 78
Arnaud, K. A. 1996, in ASP Conf. Ser. 101, Astronomical Data Analysis Software and Systems V, ed. G. H. Jacoby & J. Barnes (San Francisco, CA: ASP), 17
Ball, L., Melatos, A., Johnston, S., & Skjæ Raasen, O. 1999, ApJL, 514, L39
Barkov, M. V., & Bosch-Ramon, V. 2016, MNRAS, 456, L64
Bednarek, W., Banasiński, P., & Sitarek, J. 2018, JPhG, 45, 015201
Camilo, F., Ray, P. S., Ransom, S. M., et al. 2009, ApJ, 705, 1
Chernyakova, M., Abdo, A. A., Neronov, A., et al. 2014, MNRAS, 439, 432
Chernyakova, M., Neronov, A., Lutovinov, A., Rodriguez, J., & Johnston, S. 2006, MNRAS, 367, 1201
Chernyakova, M., Neronov, A., van Soelen, B., et al. 2015, MNRAS, 454, 1358
Coe, M. J., Okazaki, A. T., Steele, I. A., et al. 2019, MNRAS, 485, 1864
Coe, M. J., Steele, I. A., Ho, W. C. G., et al. 2017, ATel, 10920, 1
Doe, S., Nguyen, D., Stawarz, C., et al. 2007, in ASP Conf. Ser. 376, Astronomical Data Analysis Software and Systems XVI, ed. R. A. Shaw, F. Hill, & D. J. Bell (San Francisco, CA: ASP), 543
Dubus, G. 2013, A&ARv, 21, 64
Dubus, G., Guillard, N., Petrucci, P.-O., & Martin, P. 2017, A&A, 608, A59
Freeman, P., Doe, S., & Siemiginowska, A. 2001, Proc. SPIE, 4477, 76
Fruscione, A., McDowell, J. C., Allen, G. E., et al. 2006, Proc. SPIE, 6270, 62701V
Gabriel, C., Denby, M., Fyfe, D. J., et al. 2004, in ASP Conf. Ser. 314, Astronomical Data Analysis Software and Systems (ADASS) XIII, ed. F. Ochsenbein, M. G. Allen, & D. Egret (San Francisco, CA: ASP), 759
Germain, G., Milaszewski, R., McLaughlin, W., et al. 2006, in ASP Conf. Ser. 351, Astronomical Data Analysis Software and Systems XV, ed. C. Gabriel et al. (San Francisco, CA: ASP), 57
Hall, D. S. 1974, AcA, 24, 69
He, C., Ng, C.-Y., & Kaspi, V. M. 2013, ApJ, 768, 64
Ho, W. C. G., Ng, C.-Y., Lyne, A. G., et al. 2017, MNRAS, 464, 1211
Hohle, M. M., Neuhäuser, R., & Schutz, B. F. 2010, AN, 331, 349
Jennings, R. J., Kaplan, D. L., Chatterjee, S., Cordes, J. M., & Deller, A. T. 2018, ApJ, 864, 26
Johnson, T. J., Wood, K. S., Kerr, M., et al. 2018, ApJ, 863, 27
Johnston, S., Ball, L., Wang, N., & Manchester, R. N. 2005, MNRAS, 358, 1069

Johnston, S., Manchester, R. N., Lyne, A. G., et al. 1992, ApJL, 387, L37
Kargaltsev, O., Pavlov, G. G., Durant, M., Volkov, I., & Hare, J. 2014, ApJ, 784, 124
Kaspi, V. M., Roberts, M. S. E., & Harding, A. K. 2006, in Compact Stellar X-ray Sources, ed. W. H. G. Lewin & M. van der Klis (Cambridge: Cambridge Univ. Press), 279
Kolka, I., Eenmäe, T., Laur, J., & Aret, A. 2017, RNAAS, 1, 37
Krtička, J. 2014, A&A, 564, A70
Li, K. L., Kong, A. K. H., Tam, P. H. T., et al. 2017, ApJ, 843, 85
Li, K. L., Takata, J., Ng, C. W., et al. 2018, ApJ, 857, 123
Lyne, A. G., Stappers, B. W., Keith, M. J., et al. 2015, MNRAS, 451, 581
McMullin, J. P., Waters, B., Schiebel, D., Young, W., & Golap, K. 2007, in ASP Conf. Ser. 376, Astronomical Data Analysis Software and Systems XVI, ed. R. A. Shaw, F. Hill, & D. J. Bell (San Francisco, CA: ASP), 127
Melatos, A., Johnston, S., & Melrose, D. B. 1995, MNRAS, 275, 381
Miller-Jones, J. C. A., Deller, A. T., Shannon, R. M., et al. 2018, MNRAS, 479, 4849
Mukherjee, R., Gotthelf, E. V., & Halpern, J. P. 2007, Ap&SS, 309, 29
Negueruela, I., Ribó, M., Herrero, A., et al. 2011, ApJL, 732, L11
Pavlov, G. G., Hare, J., Kargaltsev, O., Rangelov, B., & Durant, M. 2015, ApJ, 806, 192
Petropoulou, M., Vasilopoulos, G., Christie, I. M., Giannios, D., & Coe, M. J. 2018, MNRAS, 474, L22
Puls, J., Vink, J. S., & Najarro, F. 2008, A&ARv, 16, 209
Rees, M. J., & Gunn, J. E. 1974, MNRAS, 167, 1
Snow, T. P., Jr. 1981, ApJ, 251, 139
Takata, J., Tam, P. H. T., Ng, C. W., et al. 2017, ApJ, 836, 241
Tam, P. H. T., He, X. B., Pal, P. S., & Cui, Y. 2018, ApJ, 862, 165
Vacca, W. D., Garmany, C. D., & Shull, J. M. 1996, ApJ, 460, 914
Wilms, J., Allen, A., & McCray, R. 2000, ApJ, 542, 914